A Novel Phase-Shift Control of Semibridgeless Active Rectifier for Wireless Power Transfer

Kerim Colak, *Member, IEEE*, Erdem Asa, *Student Member, IEEE*, Mariusz Bojarski, *Member, IEEE*, Dariusz Czarkowski, *Member, IEEE*, and Omer C. Onar, *Member, IEEE*

***Abstract*—A novel phase-shift control of a semibridgeless active rectifier (S-BAR) is investigated in order to utilize the S-BAR in wireless energy transfer applications. The standard receiver-side rectifier topology is developed by replacing rectifier lower diodes with synchronous switches controlled by a phase-shifted PWM signal. Theoretical and simulation results show that with the proposed control technique, the output quantities can be regulated without communication between the receiver and transmitter. To confirm the performance of the proposed converter and control, experimental results are provided using 8-, 15-, and 23-cm air gap coreless transformer which has dimension of 76 cm × 76 cm, with 120-V input and the output power range of 0 to 1kW with a maximum efficiency of 94.4%.**

***Index Terms*—Pickup circuit, phase shift, receiver control, resonant converter, semibridgeless active rectifier (S-BAR), wireless energy.**

I. Introduction

WIRELESS power transfer (WPT) is a growing technology to supply power to a variety of loads for which a physical contact is not convenient or possible. Potential applications include smartphone charging platforms [1]–[2], medical implant devices [3]–[4], and electric vehicle charging [5]–[6]. Starting from the transmitter side and ending at the receiver side, the contactless energy transfer system must be well designed and organized in order to achieve high efficiency [7]–[8]. However, a power flow control of wireless pickup systems is an unresolved issue where the control settings (frequency, phase shift, or dc link control, etc.) of the primary side cannot effectively control all the secondary-side outputs. A conventional pickup wireless energy transfer system is demonstrated in Fig. 1. As seen in the figure, the system consists of two main stages: the transmitter and receiver platforms. The first stage role is to deliver energy to the second stage. The dc-output voltage required by the load is provided by the second stage high-frequency rectifier and a nonisolated dc/dc converter.

Manuscript received September 30, 2014; revised December 26, 2014 and March 10, 2015; accepted April 23, 2015. Date of publication May 12, 2015; date of current version July 10, 2015. Recommended for publication by Associate Editor C. K. Lee

K. Colak was with the Polytechnic School of Engineering, New York University, Brooklyn, NY 11201, USA. He is now with Istanbul Ulasim A.S., Esenler 34220, Turkey (e-mail: kc1353@nyu.edu).

E. Asa, M. Bojarski, and D. Czarkowski are with the Polytechnic School of Engineering, New York University, Brooklyn, NY 11201, USA (e-mail: ea1145@nyu.edu; mb4496@nyu.edu; dc1677@nyu.edu).

O. C. Onar is with the Power Electronics and Electric Machinery Group, National Transportation Research Center, Oak Ridge National Laboratory, Oak Ridge, TN 37831, USA (e-mail: onaroc@ornl.gov).

Color versions of one or more of the figures in this paper are available online at http://ieeexplore.ieee.org.

Digital Object Identifier 10.1109/TPEL.2015.2430832

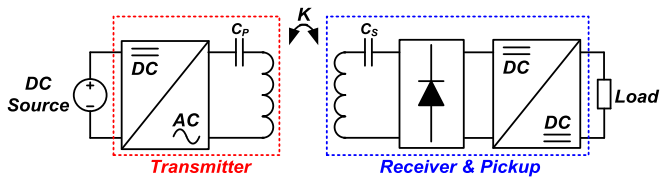

Fig. 1. Diagram of a pickup wireless energy transfer system.

Magnetic coupling, circuit parameters, and load variations cause the resonant frequency deviation in the contactless system. Thus, the output voltage of the receiver power pickup differs from its original design value. These factors cause problems for applications where a stable and regulated output voltage is required. Several pickup circuit topologies, compensation strategies, and control algorithms are explored in the literature [9]–[23]. A power management for multipickup inductive power transfer (IPT) systems is presented in [19] for materials handling applications. A new power management control approach is proposed for a parallel-tuned IPT PU circuit in that paper. The authors in [20] have investigated a multipickup bidirectional IPT by a frequency controller. A two-dimensional IPT system for mobile robots and a capacitively coupled contactless matrix charging platform are presented in [21] and [22]. Improved ac pickups for IPT systems are proposed in [23], which presents two IPT pickups, a parallel-tuned ac–ac, and a series-tuned ac–ac pickup. However, no study so far suggests any secondary-side controller without an additional receiver-side dc/dc controller and without a communication with a transmitter side.

In this paper, a novel phase-shifted semibridgeless active rectifier (S-BAR) is proposed for the WPT applications. In this topology, it is possible to control the output voltage without changing any primary-side control parameters such as frequency, duty cycle, phase angle, etc. With this property of the circuit, especially in the multipickup implementation, an independent control of each receiver ports can be achieved. In addition, the communication between the transmitter and receiver side is not necessary with the proposed control technique. In order to prove the idea and show the operating principle, a single-receiver port is considered in the paper. In the proposed secondary-side rectifier topology S-BAR, the full-bridge rectifier lower legs are replaced with synchronous rectifier (SR) switches. The SR switches are driven by a phase-shifted signal to obtain a higher voltage gain without changing the operating frequency. This novel approach results in a noncomplicated pickup topology. EMI-related problems can be reduced with this new control approach since it provides the transmitter-side control at a constant frequency. The converter model controllability is

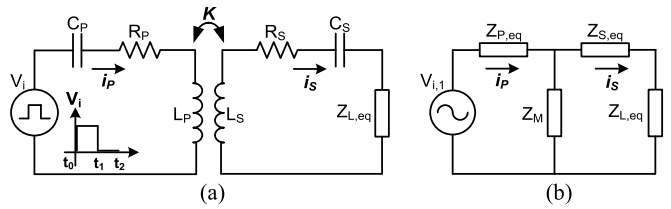

Fig. 2. Schematics of wireless power link. (a) Equivalent circuit model. (b) Simplified model.

analyzed and the transfer function of the converter is derived using MATLAB [24]–[25]. The system performance is confirmed with experimental results at 8-, 15-, and 23-cm air gaps in the coreless transformer, 150-kHz operating frequency, and a 1-kW load with a maximum efficiency of 94.4% in laboratory conditions.

II. Circuit Analysis of the Wireless Power Link

In order to perform the circuit analysis, the wireless power link can be represented as two coupled inductors and two resonant capacitors connected in series as shown in Fig. 2(a). In this model, the input voltage source is V_i, the load impedance is $Z_{L,\mathrm{eq}}$ where $Z_{L,\mathrm{eq}\prime} = \{jX_{L,\mathrm{eq}} + R_{L,\mathrm{eq}}\}$, two coupled inductors are L_P and L_S with equivalent series resistances R_S and R_P. K is a coupling factor between the two coils, and C_P and C_S are resonant capacitors. The two coupled inductors can be equivalently modeled as a transformer with proper leakage and magnetizing inductances.

To simplify analysis, both coils L_P and L_S are assumed to be identical and equal to L. Then, the model can be equivalently represented by the circuit in Fig. 2 (b). In this model, $V_{i,1}$ is a fundamental component of voltage source V_i, $Z_{P,\mathrm{eq}}$ and $Z_{S,\mathrm{eq}}$ are equivalent values where $Z_{P,\mathrm{eq}} = \{1/j\omega C_P + j\omega L_L + R_P\}$, $Z_{S,\mathrm{eq}} = \{1/j\omega C_S + j\omega L_L + R_S\}$. Z_M is the magnetizing impedance related to the coupled inductors by $Z_M = j\omega L_M$.

The model of Fig. 2 (b) is related to the model of Fig. 2(a) by the following equations:

$$\begin{aligned} L_M &= K\sqrt{L_P L_S} \\ L_L &= L - L_M = (1-K)\,L. \end{aligned} \tag{1}$$

The resonant tank square wave voltage v_i is positive during the first cycle of $[t_0, t_1]$, and during the other cycle $[t_1, t_2]$ is zero. Thus, $v_i(t)$ can be stated using Fourier analysis as

$$\begin{aligned} v_i(t) &= \begin{cases} V_i, t_0 < \omega t < t_1 \\ 0, t_1 < \omega t < t_2 \end{cases} \\ v_i(t) &= \frac{2V_i}{\pi} \sum_{n=1,3,..}^{\infty} \frac{1}{n} \sin(n\omega_{\mathrm{sw}} t). \end{aligned} \tag{2}$$

The amplitudes of the real voltage of the fundamental component of v_i and V_i are

$$v_i(t) = \frac{2V_i}{\pi} \sin(\omega_{\mathrm{sw}} t), V_{i,1} = \frac{2V_i}{\pi}. \tag{3}$$

Neglecting parasitic resistances R_P, R_S, and using the Kirchhoff's voltage law, the transmitter and receiver resonant tank in

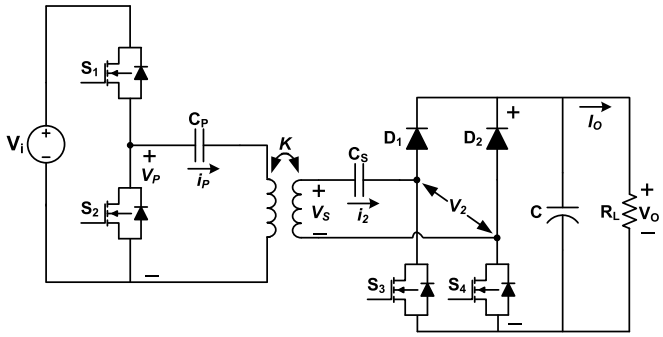

Fig. 3. Proposed phase controlled of the S-BAR.

a matrix form is

$$\begin{bmatrix} V_{i,1} \\ 0 \end{bmatrix} = \begin{bmatrix} \frac{1}{j\omega C_P} + j\omega L_L + j\omega L_M & -j\omega L_M \\ -j\omega L_M & \frac{1}{j\omega C_P} + j\omega L_L + j\omega L_M + jX_{L,\mathrm{eq}} + R_{L,\mathrm{eq}} \end{bmatrix} \begin{bmatrix} I_P \\ I_S \end{bmatrix}. \tag{4}$$

Normalized parameters help to find the transfer function of the system using design parameter values. These equations are defined and explained as follows:

$$\omega_R = \frac{1}{\sqrt{L_P C_P}}, Z_O = \sqrt{\frac{L_P}{C_P}}, Q = \frac{R_{L,\mathrm{eq}}}{Z_O}, \omega_N = \frac{\omega_{\mathrm{sw}}}{\omega_R} \tag{5}$$

where ω_R is the resonant frequency. The characteristic impedance Z_O affects the operating frequency range of the system. The quality factor Q is defined as the ratio of the total average stored energy and the dissipated energy per cycle. The normalized frequency ω_N depends on the switching ω_{sw} and resonant frequency ω_R. The voltage transfer function of the system is (6) as shown bottom of the next page

III. Analysis of the Proposed Converter

The proposed phase-control principle of an S-BAR circuit topology for the WPT is shown in Fig. 3 [26]–[27]. It comprises a half-bridge resonant inverter with an input dc source V_i, an air gap coreless transformer with resonant capacitors C_P and C_S, and a single-phase semibridge rectifier in the secondary side. The inverter is composed of switches S_1 and S_2, the resonant tank voltage V_P, and the resonant tank current I_P. The active rectifier is comprised of two transistors S_3 and S_4 with antiparallel diodes in the lower part of switching legs and two diodes D_1 and D_2 in the upper parts. The phase-shift angle of the secondary-side transistors regulates the output voltage V_O and power in the load R_L. The secondary-side voltage is denoted here as V_S, the secondary-side current is I_S, and the voltage across the rectifier tap center (receiver rectifier voltage) is V_2.

The operating waveforms and switch state transitions are presented in Figs. 4 and 5 to show the behavior of the proposed converter. To simplify the circuit analysis, secondary-side

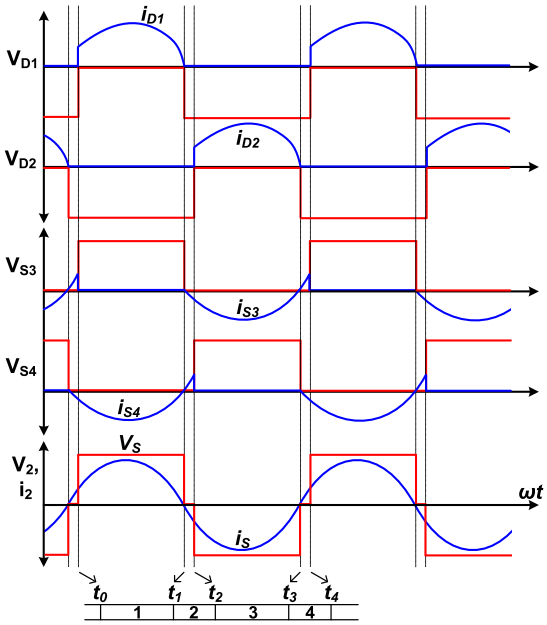

Fig. 4. Voltage and current waveforms in the switch and diodes.

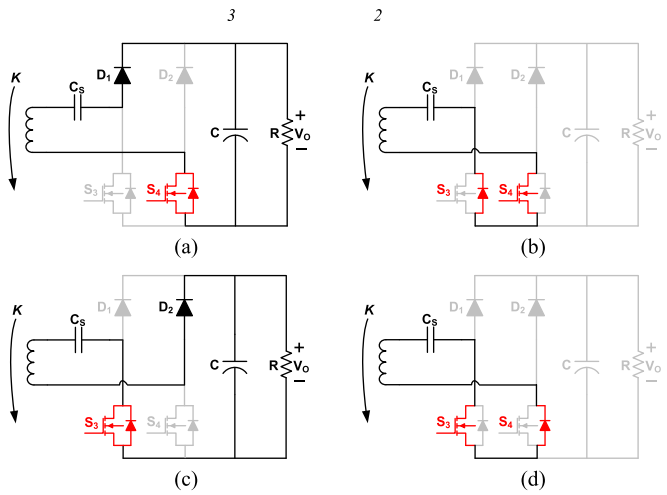

Fig. 5. Mode analysis, current path, and switching transition in the receiver side. (a) Mode 1, (b) Mode 2, (c) Mode 3, (d) Mode 4.

rectifier diodes and switches are ideal, the output capacitor is assumed to be large enough for a constant dc output, and filter losses are neglected. The proposed circuit is examined under these conditions in the following operation modes.

Mode 1 [$t_0 < t < t_1$]: During this interval, the rectifier switch S_4 is turned ON and diode D_1 is in on-state. As shown in Fig. 4, the cycle starts with positive current i_S and the current flows through D_1 and S_4 in the converter as depicted in Fig. 5(a).

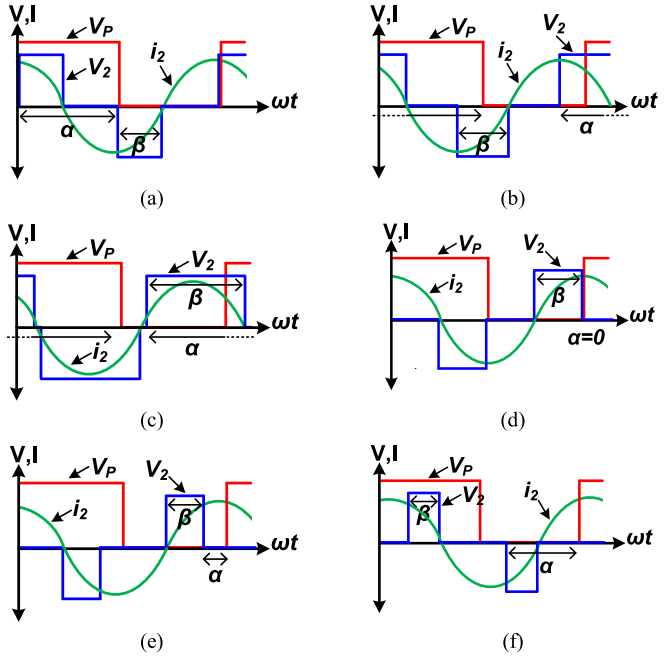

Fig. 6. Resonant tank and transformer voltage and current waves at different α and β. (a) $\alpha = -\pi$ and $\beta < a$, (b) $-\pi \leq \alpha \leq -\pi/2$ and $\beta < \alpha$, (c) $-\pi/2 \leq \alpha \leq 0$, and $\beta < \alpha$, (d) $\alpha = 0$ and $\beta > \alpha$, (e) $0 \leq \alpha \leq \pi/2$ and $\beta > \alpha$, (f) $\pi/2 \leq \alpha \leq \pi$ and $\beta < \alpha$.

Mode 2 [$t_1 < t < t_2$]: The current flows in negative direction in this mode through the antiparallel diode of switch S_3 and switch S_4 as shown in Fig. 5 (b). Both diodes are negative biased and the secondary side is shorted with the antiparallel diode of switch S_3 and switch S_4. The current wave is demonstrated in Fig. 4.

Mode 3 [$t_2 < t < t_3$]: The resonant current further decreases in this interval and reaches the minimum value within this mode as plotted in Fig. 4. The switch S_3 is ON, while diode D_1 is OFF and D_2 is in the on-state. The current flows from the coreless transformer to the receiver side switch S_3 and diode D_2 as shown in Fig. 5 (c).

Mode 4 [$t_3 < t < t_4$]: The current flows in the positive direction in the resonant tank, and the receiver side switch S_3 and the antiparallel diode of switch S_4 are shorted as shown in Fig. 5 (d). Both diodes are reverse biased and switch S_3 and the antiparallel diode of switch S_4 are in the conduction mode. The current wave is demonstrated in Fig. 4. After this interval, the modes are completed and the inverter continues with Mode 1 again.

IV. Semibridgeless Technology

The receiver rectifier voltage V_2 and current waveforms i_2 are shown with different conduction angle β in Fig. 6. The phase controller angle α indicates the period of time between rising edge of the rectifier voltage V_2 and decreasing edge of

$$M_V = \left| \frac{(R_{L,\mathrm{eq}} + jX_{L,\mathrm{eq}})\, j\omega_N K Z_O}{\frac{1-\omega_N(1-K)Z_O}{1-\omega_N^2} - \frac{[1-\omega_N(1-K)]Z_O^2(1-\omega_N^2)}{\omega_N^2} + \frac{(1-\omega_N^2)(R_{L,\mathrm{eq}}+jX_{L,\mathrm{eq}})}{j\omega_N}} \right| \quad (6)$$

the primary resonant tank voltage V_P. This controller forms the rectifier conduction angle β and determines the output voltage V_O. The cases in Fig. 6(a)–(f) can occur at different β, the coreless transformer coupling coefficient factor *K*, and the load resistance *(R_L)*. In other words, even if α is kept constant, β varies with different *K* and R_L. It is important to mention that the converter operation should be avoided in some stages because of a very high output power. This is discussed in more details in the following sections. In this part, the phase-shift operations are considered at a constant frequency.

Controlling α and β is important to achieve various operating conditions. For -$\pi \leq \alpha \leq \pi$, β is being changed as shown in the figure. When the current i_2 is leading the receiver rectifier voltage V_2 as seen in Fig. 6(a), (b), (c), and (f), β increases and reaches the maximum value as depicted in Fig. 6(c). At this moment, the active switches allow more current to pass, thus raising the output voltage. Another condition happens when the current is lagging the voltage after the maximum value point as shown in Fig. 6(d) and (e). Decreasing the conduction angle β prevents the current from passing to the output and thus lowers the output voltage. The other important thing at this cycle is that β is decreasing but α is increasing. It means that the conduction angle can be in inverse or direct proportion to the controller angle α. By varying the amount of time in which current reaches the output, the output voltage can be regulated depending on the control angle α and the conduction angle β. It is important to explain that positive or negative sign of the receiver rectifier voltage and current phase difference Θ indicates the load is inductive or capacitive; therefore, the reflected impedance of the receiver is shown as an inductive $\Theta > 0$, and as a capacitive $\Theta < 0$.

As seen in Fig. 6, there are three possible stages, $-V_O$, *0*, and V_O for the receiver-side voltage which is determined by the state of rectifier side switches. The circuit operation is described by considering inductive and capacitive load conditions in subsequent paragraphs.

For the inductive load

$$v_2(\omega t) = \begin{cases} 0, -\alpha < \omega t < (\pi - \alpha - \beta) \\ -V_O, (\pi - \alpha - \beta) < \omega t < (\pi - \alpha) \\ 0, (\pi - \alpha) < \omega t < (2\pi - \alpha - \beta) \\ V_O, (2\pi - \alpha - \beta) < \omega t < (2\pi - \alpha) \end{cases}. \quad (7)$$

The corresponding voltage value on the receiver terminals can be derived using the first harmonic approximation (FHA) as

$$v_{2,1} = \frac{4V_O}{\pi} \sin\left(\frac{\beta}{2}\right) \sin\left(\omega t + \alpha + \frac{\beta}{2} - \frac{3\pi}{2}\right). \quad (8)$$

The output current can be also derived in a similar way with the above expression

$$i_2(\omega t) = I_2 \sin(\omega t + \alpha + \beta - 2\pi) \quad (9)$$

The equivalent impedance is obtained by taking the ratio of $v_{2,1}$ and i_2 in the frequency domain, and is given by

$$Z_{L,\mathrm{eq}} = \frac{4}{\pi^2} R_L (1 - \cos\beta) \sin\left(\frac{\beta}{2}\right) e^{j\left[\frac{\pi}{2} - \frac{\beta}{2}\right]}. \quad (10)$$

Taking real and imaginary portions of (10), the equivalent resistance and reactance values are obtained as

$$\begin{aligned} R_{L,\mathrm{eq}} &= Re\left\{\frac{4}{\pi^2} R_L (1 - \cos\beta) \sin\left(\frac{\beta}{2}\right) e^{j\left[\frac{\pi}{2} - \frac{\beta}{2}\right]}\right\} \\ &\quad 0 \leq \beta \leq \pi \\ X_{L,\mathrm{eq}} &= Im\left\{\frac{4}{\pi^2} R_L (1 - \cos\beta) \sin\left(\frac{\beta}{2}\right) e^{j\left[\frac{\pi}{2} - \frac{\beta}{2}\right]}\right\} \\ &\quad 0 \leq \beta \leq \pi \end{aligned} \quad (11)$$

$Z_{L,\mathrm{eq}}$ is inductive and the load angle *(π/2–β/2)* is always positive.

For the capacitive load

$$v_2(\omega t) = \begin{cases} -V_O, -\alpha < \omega t < (-\alpha + \beta) \\ 0, (-\alpha + \beta) < \omega t < (\pi - \alpha) \\ V_O, (\pi - \alpha) < \omega t < (\pi - \alpha + \beta) \\ 0, (\pi - \alpha + \beta) < \omega t < (2\pi - \alpha) \end{cases}. \quad (12)$$

FHA analysis results in the corresponding voltage value on the receiver terminals

$$v_{2,1} = \frac{4V_O}{\pi} \sin\left(\frac{\beta}{2}\right) \sin\left(\omega t + \alpha - \frac{\beta}{2} - \frac{\pi}{2}\right). \quad (13)$$

With the above expression, the output current can be obtained

$$i_2(\omega t) = I_2 \sin(\omega t + \alpha - \beta). \quad (14)$$

The equivalent impedance $Z_{L,\mathrm{eq}}$ can be defined as

$$Z_{L,\mathrm{eq}} = \frac{4}{\pi^2} R_L (1 - \cos\beta) \sin\left(\frac{\beta}{2}\right) e^{j\left[\frac{\beta}{2} - \frac{\pi}{2}\right]}. \quad (15)$$

The equivalent resistance and reactance values are acquired from the above equation as

$$\begin{aligned} R_{L,\mathrm{eq}} &= Re\left\{\frac{4}{\pi^2} R_L (1 - \cos\beta) \sin\left(\frac{\beta}{2}\right) e^{j\left[\frac{\beta}{2} - \frac{\pi}{2}\right]}\right\} \\ &\quad -\pi \leq \beta \leq 0 \\ X_{L,\mathrm{eq}} &= Im\left\{\frac{4}{\pi^2} R_L (1 - \cos\beta) \sin\left(\frac{\beta}{2}\right) e^{j\left[\frac{\beta}{2} - \frac{\pi}{2}\right]}\right\} \\ &\quad -\pi \leq \beta \leq 0 \end{aligned} \quad (16)$$

The load angle *(β/2–π/2)* is always negative and $Z_{L,\mathrm{eq}}$ is capacitive. Fig. 7 shows the load equivalent resistance $R_{L,\mathrm{eq}}$ and reactance $X_{L,\mathrm{eq}}$ as a function of β and load resistance R_L.

V. Power Loss Estimation

The wireless power link analysis is performed based on the circuit shown in Fig. 2. As the first step of the analysis, the total input impedance Z_{in} seen by the ac source is calculated

$$Z_{\mathrm{in}} = j\omega_N K Z_O + \frac{(j\omega_N K Z_O)^2}{\frac{1}{K}\left(1 - \frac{1}{\omega_N^2}\right) + \frac{X_{L,\mathrm{eq}}}{\omega K L_P} + \frac{Q}{jK\omega_N}} + \frac{\left(1 - [1 - K]\,\omega_N^2\right) Z_O}{j\omega_N}. \quad (17)$$

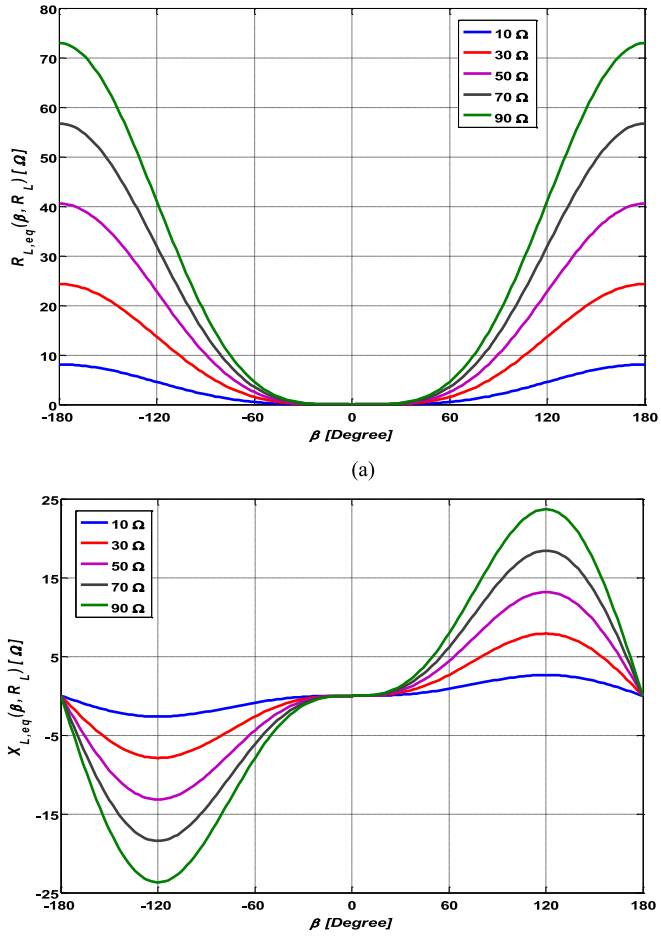

Fig. 7. Equivalent load impedance variation with conduction angle β and load resistance R_L for (a) equivalent resistance $R_{L,\mathrm{eq}}$ and (b) equivalent reactance $X_{L,\mathrm{eq}}$.

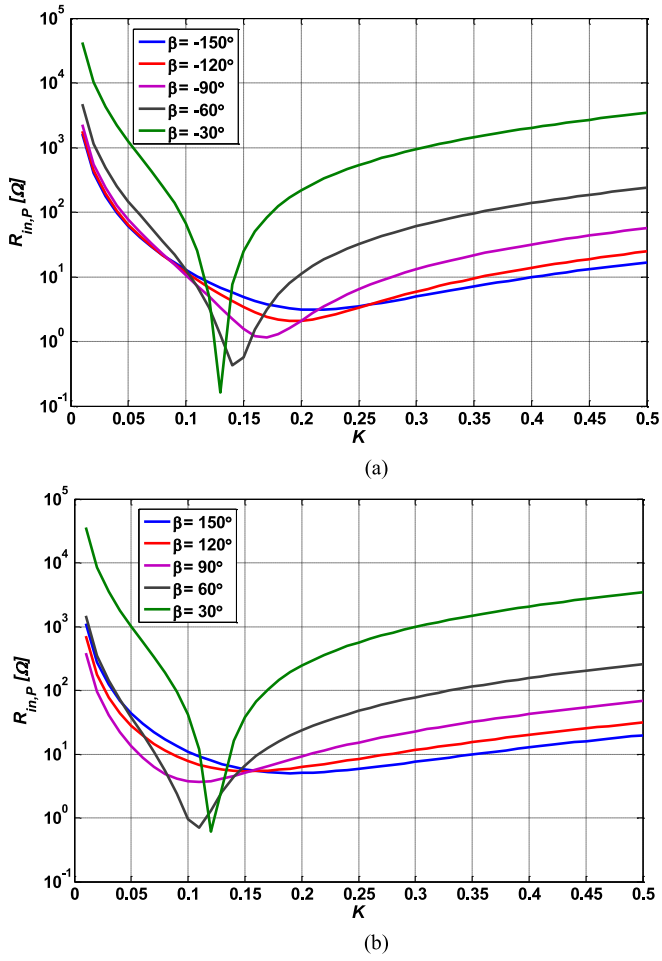

Fig. 8. Primary-side-reflected parallel resistance $R_{\mathrm{in},P}$ with coupling K and conduction angle β for (a) $\beta < 0$ and (b) $\beta > 0$.

The primary-side reflected parallel resistance $R_{\mathrm{in},P}(=|Z_{\mathrm{in}}|^2/Re\{Z_{\mathrm{in}}\})$ is given as a function of K and β in Fig. 8.

Using the total input impedance, the primary-side current is equal to

$$I_P = \frac{V_{i,1}}{Z_{\mathrm{in}}}. \tag{18}$$

Then, the secondary-side current can be calculated as

$$I_S = \frac{V_{i,1}}{\frac{1}{K}\left(1-\frac{1}{\omega_N^2}\right) j\omega_N Z_O + \frac{1}{K}\left(1-\frac{1}{\omega_N^2}\right)\frac{Q+jX_{L,\mathrm{eq}}}{Z_O} Z_O - j\omega_N Z_O K}. \tag{19}$$

The primary and the secondary currents ratio is

$$\frac{I_P}{I_S} = \frac{1}{K}\left(1-\frac{1}{\omega_N^2}\right) + \frac{X_{L,\mathrm{eq}}}{\omega K L_P} + \frac{Q}{jK\omega_N}. \tag{20}$$

In order to calculate the efficiency of the circuit, equations for the losses and the output power are needed. The output power can be calculated based on the secondary-side current as

$$P_O = \frac{|I_S|^2 R_{L,\mathrm{eq}}}{2}. \tag{21}$$

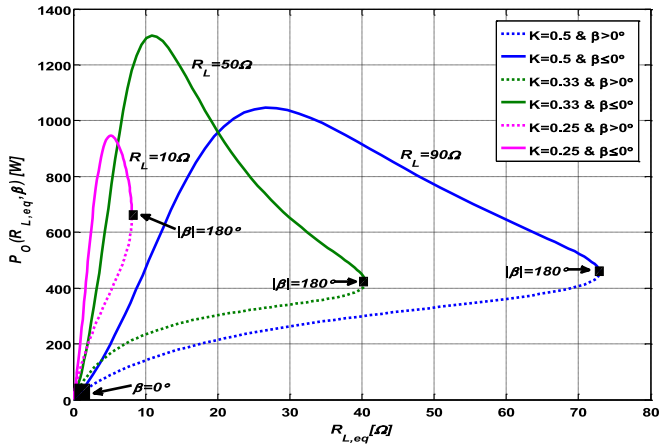

Fig. 9. Output power P_O analysis with equivalent resistance $R_{L,\mathrm{eq}}$ and conduction angle β by various R_L and coupling K.

The output power analysis with β, and $R_{L,\mathrm{eq}}$ and various K and R_{L} are shown in Fig. 9.

The circuit conduction losses can be calculated based on the currents. The conduction losses are related to the real parts of the impedances Z_P and Z_S, which are R_P and R_S. It can be seen that these impedances can also include additional components, for instance, lead cables which makes this analysis more general.

The circuit losses are calculated using the following equation:

$$P_C = \frac{|I_P|^2 R_P + |I_S|^2 R_S}{2}. \tag{22}$$

Switching and switch conduction losses of the transmitter can be calculated using the following equations:

$$P_{S,T} = \frac{\omega}{2\pi} V_i \left|I_P \sin(\theta)\right| \left(\frac{2t_r}{3} + t_f\right) \tag{23}$$

$$P_{S,C,T} = \frac{r_{\rm DS} I_P^2}{2} \tag{24}$$

where θ is the phase difference between the voltage and current signal in the transmitter resonant tank, $r_{\rm DS}$ is the on-state resistance of switches, t_f is the turning off current fall time, and t_r is the voltage rise time. The S-BAR switching losses, switch conduction losses, and diode conduction losses can be expressed as, respectively

$$P_{S,R} = \frac{2\omega}{\pi} \frac{V_O^2}{R_L} \left[-\tan\left(\frac{|\beta|}{2}\right)\right]^{-1} \left(\frac{2t_r}{3} + t_f\right)$$

$$P_{S,C,R} = \frac{1}{\pi}\int_0^{\pi} V_D i_2 \mathrm{d}t + \frac{1}{\pi}\int_0^{\pi} r_{\rm DS} i_2^2 \mathrm{d}t \tag{25}$$

$$= \frac{V_D V_O}{R_L}\left[\tan^2\left(\frac{\beta}{2}\right)\right]^2 + \frac{1}{2}\left(\frac{\sqrt{r_{\rm DS}}\pi V_O}{R_L(1-\cos\beta)}\right)^2 \tag{26}$$

$$P_{D,C,R} = \frac{1}{2\pi}\int_0^{2\pi} V_F i_2 \mathrm{d}t + \frac{1}{\pi}\int_0^{\beta} r_D i_2^2 \mathrm{d}t$$

$$= \frac{V_F V_O}{R_L} + \left(\frac{\sqrt{\pi r_D} V_O}{R_L(1-\cos\beta)}\right)^2 \times \frac{1}{4}(2\beta - \sin(2\beta)) \tag{27}$$

where V_D is the switch internal diode forward voltage drop and V_F is the diode forward voltage drop. The overall efficiency of the system can be estimated by

$$\eta = P_O / (P_O + P_C + P_{S,T} + P_{S,C,T} + P_{S,R} + P_{S,C,R} + P_{D,C,R}). \tag{28}$$

Neglecting switching losses, effects of β and $R_{L,eq}$ on the efficiency of the converter at various K and $R_{\rm L}$ are presented in Fig. 10.

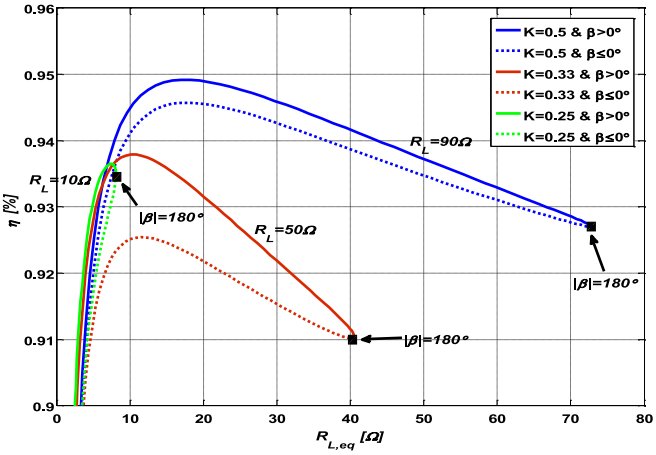

Fig. 10. Efficiency η estimation with equivalent resistance $R_{L,\rm eq}$ and conduction angle β under different coupling K and load R_L.

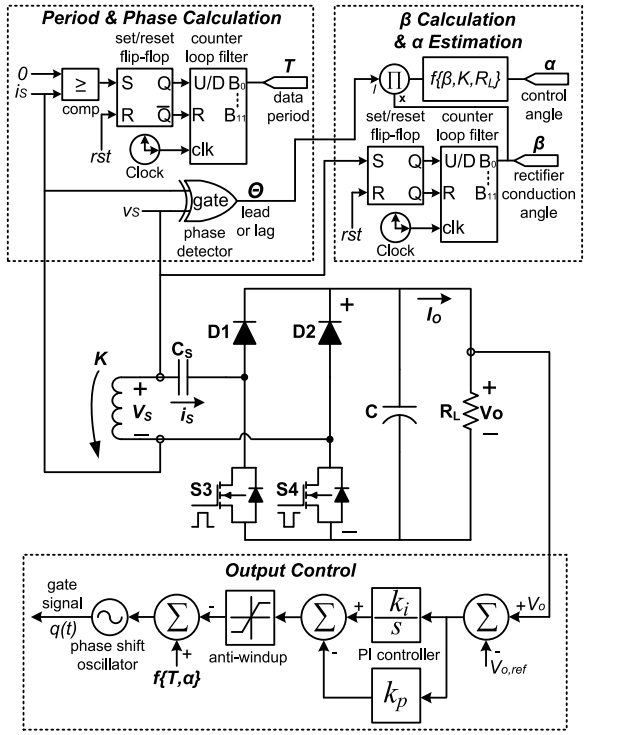

Fig. 11. Control block diagram of the system with the output voltage and receiver input voltage, and current sensing.

VI. Proposed Phase-Shift Control Analysis

Due to small complexity of the S-BAR converter, the control of the system is relatively simpler than utilization of communication devices for the misalignment or position/distance determination and additional dc/dc converter stages in the receiver side. In this proposed approach, communication between the transmitter and receiver sides is not necessary. Only voltage and current signals at the receiver inputs and voltage sensing at the output are sufficient to control the system by generating two phase-shifted PWM pulses.

The proposed phase-shift approach to the S-BAR control is shown in Fig. 11. The designed control is implemented in FPGA and a microprocessor. The system operating frequency *(1/T)*, the phase difference detection between receivers input voltage and current Θ, and the secondary-side rectifier conduction angle β are determined by an FPGA block. Additionally, high voltage, current, and temperature protection are ensured by FPGA. The control angle α estimation is carried by a microprocessor with β, coupling coefficient factor K, and load R_L as parameters and considering voltage and current phase detection Θ to use the right set of equations (inductive or capacitive load). For the system control, α determination is important to manage the output at the load terminals. It can be seen that system

TABLE I
PROPOSED CONVERTER PARAMETERS

Symbol	Parameter	Value
V_i	dc-input voltage	120 V
V_O	dc-output voltage range	0–100 V
I_O	maximum output current	10 A
P_O	maximum output power	1 kW
C_P , C_S	resonant capacitors	40 nF
L_P , L_S	coil self-inductances	25 μH
d	square coil dimension	76 cm $\times$ 76 cm
n	coil turn number	4
f_{sw}	operating frequency	150 kHz

control can be achieved without the knowledge of transmitter-side parameters. Depending on the inductive and capacitive load condition, the output current phase (ϕ_2) can be described by using (9) and (14) as follows:

$$\phi_2 = \begin{cases} \alpha + \beta - 2\pi, & \Theta > 0 \\ \alpha - \beta, & \Theta < 0 \end{cases}. \tag{29}$$

Using (4), the value of ϕ_2 can be determined with the following equation:

$$\phi_2 = -\pi - \tan^{-1}\left(\frac{|Z_q|\,\pi^2}{8R_L \sin\left(\frac{\beta}{2}\right)^4} + \tan\left(\frac{\beta}{2}\right)^{-1}\right). \tag{30}$$

Considering conditions above, α parameter is calculated as

$$\alpha = -\pi + \left[-\beta - \tan^{-1}\left(\frac{|Z_q|\,\pi^2}{8R_L \sin\left(\frac{\beta}{2}\right)^4} + \tan\left(\frac{\beta}{2}\right)^{-1}\right)\right], \quad \Theta > 0 \tag{31}$$

$$\alpha = -\pi + \left[\beta - \tan^{-1}\left(\frac{|Z_q|\,\pi^2}{8R_L \sin\left(\frac{\beta}{2}\right)^4} + \tan\left(\frac{\beta}{2}\right)^{-1}\right)\right], \quad \Theta < 0 \tag{32}$$

where $Z_q = [1/j\omega C_P + j\omega L_L]j\omega L_M/(1/j\omega C_P + j\omega L_P) + j\omega L_L + 1/j\omega C_S$ is compared to the measured results in the next section. Based on the Z_q impedance and the β angle, the α angle can be obtained as given by (31) and (32). Here, α can have two values, depending on the sign on Θ.

VII. EXPERIMENTAL RESULTS

The proposed wireless system is designed for 1-kW, 120-V input voltage, and 0–100 V output voltage rating as a laboratory prototype. The coreless transformer is tested with 3-, 6-, and 9-in distances between coils which results in 0.5, 0.33, and 0.25 coupling factor, respectively. The topology parameters of the converter are given in Table I.

Experimental measurements and calculated results are quite similar with different *K* values as shown in Fig. 12 (a), (b), and (c). Also, different *K* coefficients do not significantly affect the system control as seen in Fig. 12(d). Therefore, estimation can be calculated neglecting *K* factor. With the estimated α at the receiver side, the output voltage of the system can be regulated by synchronizing the operating frequency. The control angle is evaluated by the output voltage with its reference value. When the voltage feedback signal error comes to zero, the system control is achieved.

The characteristic waveforms of the proposed converter described in Sections III and IV are given to verify the circuit operation. Selected current and voltage waveforms at different control angles with different coupling factors are given in Fig. 13. The phase-shift angle controls the output voltage by changing the transformer secondary-side voltage as shown in the figure.

Fig. 14 shows the output power characteristics versus the phase-shift angle with different *K* values. When the switching frequency is constant at 150 kHz, the phase-shift angle is swept to obtain the output voltage waveform at each different *K*. As seen in the figure, the output voltage changes in two regions when the phase-shift angle is lower than zero in the first region *($\alpha < 0$)* and greater than zero *($\alpha > 0$)* in the second region. The wide output power range 0 to 200 W, 0 to 500 W, and 0 to 1 kW can be achieved in these two regions. The other important observation from the results is that the maximum output power increases with decreasing the coupling coefficient factor *0.25 < K < 0.5* at 150-kHz operating frequency. This condition can be explained with an input impedance (17) in Section V. The equivalent parallel input resistances are depicted when $\beta < 0$ and $\beta > 0$ in Fig. 8 (a) and (b), respectively. As seen from the figures, the system coupling coefficient *K* changes the input parallel resistance $R_{\text{in},P}$ with β. The lower resistances mean that the source is loaded heavily. If the coupling is very poor, the desired active power cannot be transferred to the output load.

The efficiency characteristics of the proposed topology versus the phase-shift angle with different *K* are given in Fig. 15. The efficiency of the converter is greater than 80% in all different couplings when the phase shift is $\alpha < 0$. The reflected parallel resistance gets high when *K* increases above 0.25 which results in lower input current. As described power loss equations in (21)–(27), they depend on the current. Thus, the efficiency is improved when *K* increases above 0.25. The maximum efficiency reaches 94.4% at 0.5 coupling with the phase-shift angle being around $-90°$. Considering the output power characteristic at the constant load in the experimental results, the variable voltage range of 25 to 50 V, 40 to 80 V, and 50 to 100 V can be achieved with a high efficiency for $\alpha < 0$. The operation at $\alpha > 0$ yields low efficiency and should be avoided because of the high circulating current and hard switching conditions.

The conventional wireless system as shown in Fig. 1 and the proposed converter performances are compared in Fig. 16. The conventional wireless system is operated at the constant frequency with an additional dc/dc stage of a secondary-side controller converter described in [28]. The comparison is realized with different coupling coefficient *K* factors at the

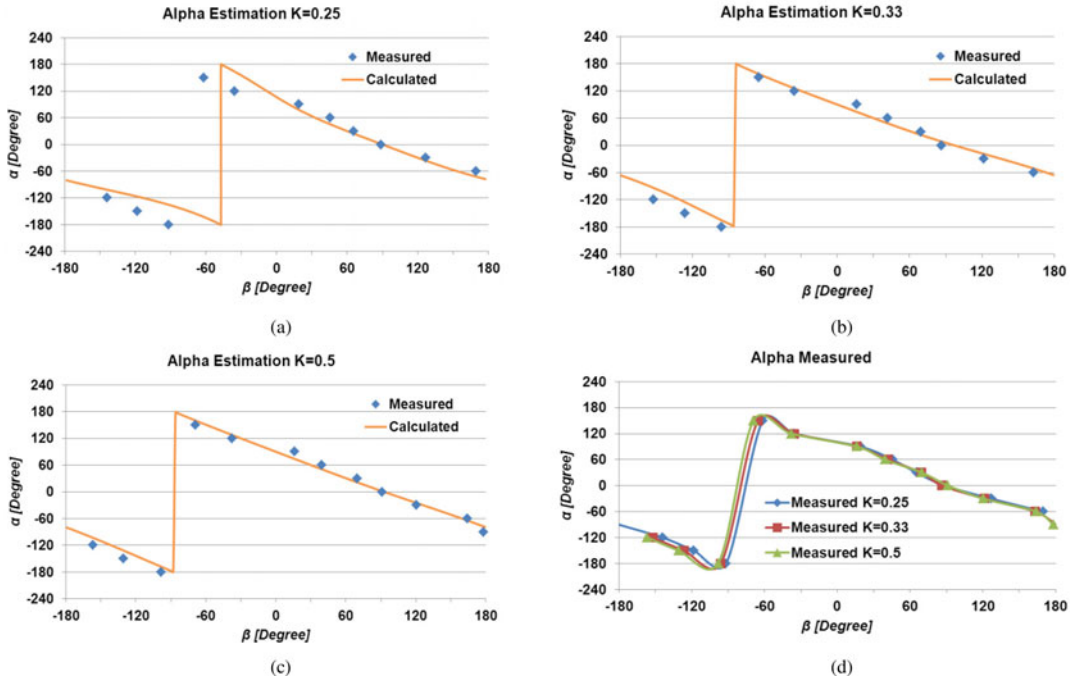

Fig. 12. System controller estimation comparison with analytical and experimental results. (a) $K = 0.25$, (b) $K = 0.33$, (c) $K = 0.5$, (d) experimental results with different couplings $K = 0.25$, $K = 0.33$, $K = 0.5$.

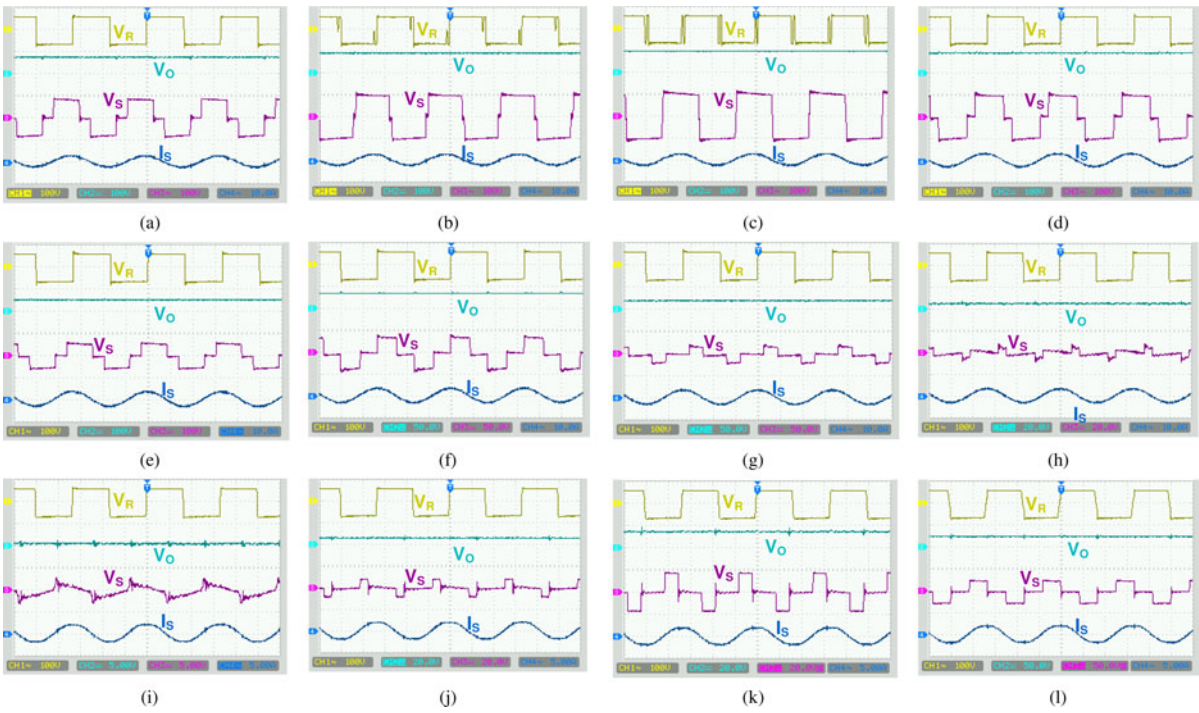

Fig. 13. Resonant tank voltage (V_R), current (I_R), and secondary-side voltage (V_S), current (I_S) waveforms with different coupling coefficient (K) and phase-shift control angle (α). (a) $K = 0.25$, $\alpha = -30°$, (b) $K = 0.25$, $\alpha = -60°$, (c) $K = 0.25$, $\alpha = -90°$, (d) $K = 0.25$, $\alpha = -120°$, (e) $K = 0.3$, $\alpha = -150°$, (f) $K = 0.3$, $\alpha = -180°$, (g) $K = 0.3$, $\alpha = 150°$, (h) $K = 0.3$, $\alpha = 120°$, (i) $K = 0.5$, $\alpha = 90°$, (j) $K = 0.5$, $\alpha = 60°$, (k) $K = 0.5$, $\alpha = 30°$, (l) $K = 0.5$, $\alpha = 0°$.

same operating frequency and the same load conditions. The proposed converter performance is better than the conventional type in all load conditions as depicted in Fig. 16. The comparison result summarized in Table II shows that the overall efficiency is improved by 7% considering the different coupling conditions for $K = 0.25$, 0.3, and 0.5. The other advantage of the proposed converter is its lower volume since it eliminates the traditional system bulky and heavy components of an additional dc/dc stage in the secondary side. This also reduces the system cost.

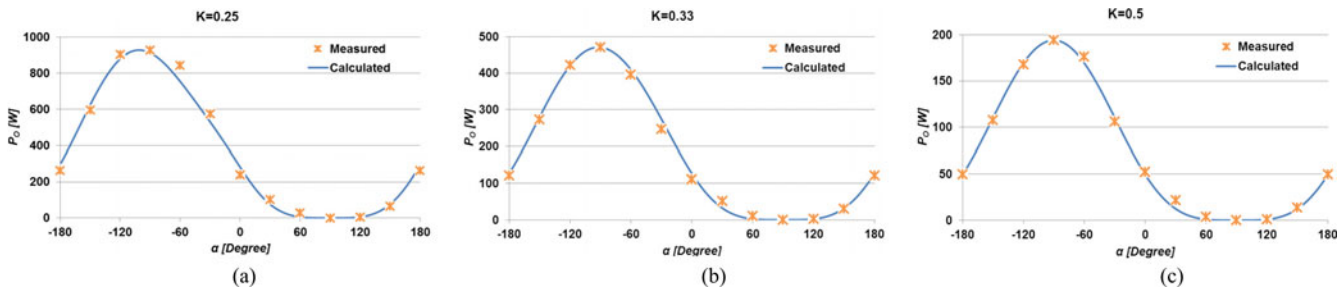

Fig. 14. Comparison of measured and calculated power as a function of the control phase angle with different K's. (a) $K = 0.25$, (b) $K = 0.33$, (c) $K = 0.5$.

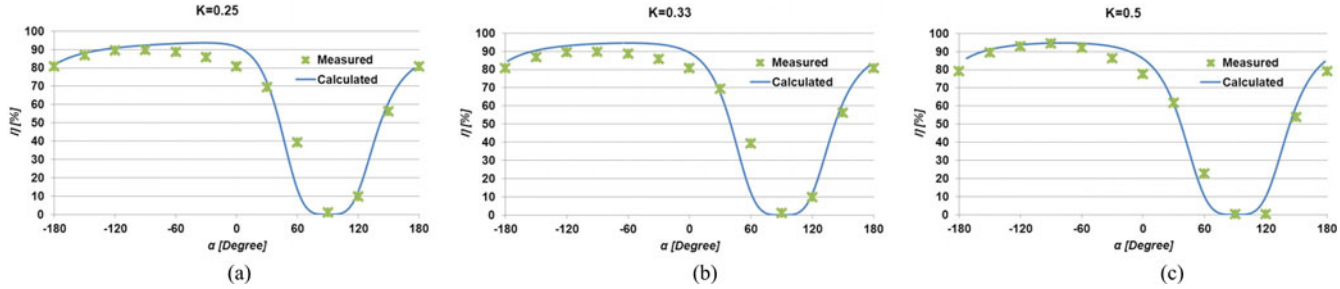

Fig. 15. Comparison of measured and calculated efficiency as a function of the control phase angle with different K's. (a) $K = 0.25$, (b) $K = 0.33$, (c) $K = 0.5$.

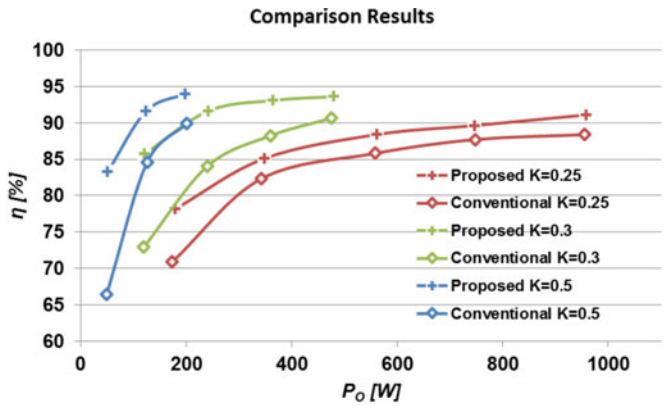

Fig. 16. Efficiency comparison of the proposed converter with a conventional converter in [26] for the different coupling coefficient conditions $K = 0.25$, 0.33, and 0.5.

TABLE II
COMPARISON OF THE PROPOSED CONVERTER WITH THE CONVENTIONAL TYPE

	Conventional [30]	Proposed
Control	Secondary	Secondary
Control Type	Duty Cycle	Phase Shift
Additional dc/dc Stage	Yes	No
Average Efficiency	≈82%	≈89%

VIII. CONCLUSION

In this study, a new phase-shift control of an S-BAR is presented for WPT applications. With the proposed control, the communication between the transmitter and receiver side is not required. The simple converter topology has reduced number of switches on the secondary side as compared to typical inductive energy transfer secondary-side dc/dc converter topologies. The converter model analysis with steady-state equivalent circuits is given using FHA, and voltage/current waveforms are presented for all operating modes. The transfer function of the converter is also derived analytically. Conduction losses, switching losses, and efficiency estimation are provided considering the transmitter and receiver side of the wireless converter. The proposed control strategy adjusts the output voltage of the system by phase-shift tuning of the active switches in the receiver. The concepts presented here can be also used in multiple output receiver wireless applications since the output control can be regulated only in the receiver side. The proposed receiver topology utilization can also be facilitated for the impedance matching protection by adjusting reflected equivalent resistance value. The system performance is confirmed with theoretical and experimental results at various coupling coefficient factors. To verify the proposed phase-shifted S-BAR converter, it is designed for 1-kW maximum power at 120-V input. The laboratory prototype achieved a 94.4% maximum efficiency.

REFERENCES

[1] Y. Jang and M. M. Jovanovic, "A contactless electrical energy transmission system for portable telephone battery chargers," *IEEE Trans. Ind. Electron.*, vol. 50, no. 3, pp. 520–527, Jun. 2003.

[2] K. C. Wan, Q. Xue, X. Liu, and S. Y. Hui, "Passive radio frequency repeater for enhancing signal reception and transmission in a wireless charging platform," *IEEE Trans. Ind. Electron.*, vol. 61, no. 4, pp. 1750–1757, Apr. 2014.

[3] A. K. Ram-Rakhyani and G. Lazzi, "On the design of efficient multi coil telemetry system for biomedical implants," *IEEE Trans. Biomed. Circuits Syst.*, vol. 7, no. 1, pp. 11–23, Feb. 2013.

[4] M. Q. Nguyen, Z. Hughes, P. Woods, Y. S. Seo, S. Rao, and J. C. Chiao, "Field distribution models of spiral coil for misalignment analysis in wireless power transfer systems," *IEEE Trans. Microw. Theory Tech.*, vol. 62, no. 4, pp. 920–930, Apr. 2014.

[5] U. K. Madawala, M. Neath, and D. J. Thrimawithana, "A power frequency controller for bidirectional inductive power transfer systems," *IEEE Trans. Ind. Electron.*, vol. 60, no. 1, pp. 310–317, Jan. 2013.

[6] F. Musavi and W. Eberle, "Overview of wireless power transfer technologies for electric vehicle battery charging," *IET Power Electron.*, vol. 7, no. 1, pp. 60–66, Jan. 2014.
[7] W. Zhang, S. C. Wong, C. K. Tse, and Q. Chen, "Design for efficiency optimization and voltage controllability of series compensated inductive power transfer systems," *IEEE Trans. Power Electron.*, vol. 29, no. 1, pp. 191–200, Jan. 2014.
[8] C. Florian, F. Mastri, R. P. Paganelli, D. Masotti, and A. Costanzo, "Theoretical and numerical design of a wireless power transmission link with GaN based transmitter and adaptive receiver," *IEEE Trans. Microw. Theory Tech.*, vol. 62, no. 4, pp. 931–946, Apr. 2014.
[9] W. Zhang, S. Wong, C. Tse, and Q. Chen, "An optimized track length in roadway inductive power transfer systems," *IEEE J. Emerg. Sel. Topics Power Electron.*, vol. 2, no. 3, pp. 598–608, Sep. 2014.
[10] J. Huh, S. W. Lee, W. Y. Lee, G. H. Cho, and C. T. Rim, "Narrow-width inductive power transfer system for online electrical vehicles," *IEEE Trans. Power Electron.*, vol. 26, no. 12, pp. 3666–3679, Dec. 2011.
[11] G. Elliott, S. Raabe, G. A. Covic, and J. T. Boys, "Multiphase pickups for large lateral tolerance contactless power-transfer systems," *IEEE Trans. Ind. Electron.*, vol. 57, no. 5, pp. 1590–1598, May 2010.
[12] G. A. Covic, J. T. Boys, A. M. W. Tam, and J. C. H. Peng, "Self tuning pick-ups for inductive power transfer," in *Proc. IEEE Power Electron. Spec. Conf.*, Jun. 2008, pp. 3489–3494.
[13] P. Si, A. P. Hu, S. Malpas, and D. Budgett, "Switching Frequency analysis of dynamically detuned ICPT power pick-ups," in *Proc. Int. Conf. Power Syst. Technol.*, Oct. 2006, pp. 1–8.
[14] J. U. W. Hsu, A. P. Hu, and A. Swain, "A wireless power pickup based on directional tuning control of magnetic amplifier," *IEEE Trans. Ind. Electron.*, vol. 56, no. 7, pp. 2771–2781, Jul. 2009.
[15] Z. Pantic and S. M. Lukic, "Framework and topology for active tuning of parallel compensated receivers in power transfer systems," *IEEE Trans. Power Electron.*, vol. 27, no. 11, pp. 4503–4513, Nov. 2012.
[16] H. H. Wu, G. A. Covic, J. T. Boys, and D. J. Robertson, "A series tuned inductive power transfer pickup with a controllable ac voltage output," *IEEE Trans. Power Electron.*, vol. 26, no. 1, pp. 98–109, Jan. 2011.
[17] U. K. Madawala, M. Neath, and D. J. Thrimawithana, "A power frequency controller for bidirectional inductive power transfer systems," *IEEE Trans. Ind. Electron.*, vol. 60, no. 1, pp. 310–317, Jan. 2013.
[18] D. J. Thrimawithana, U. K. Madawala, and M. Neath, "A synchronization technique for bidirectional IPT systems," *IEEE Trans. Ind. Electron.*, vol. 60, no. 1, pp. 301–309, Jan. 2013.
[19] L. Chen, J. Boys, and G. Covic, "Power management for multiple-pickup IPT systems in materials handling applications," *IEEE J. Emerg. Sel. Topics Power Electron.*, vol. 3, no. 1, pp. 163–176, Mar. 2015.
[20] A. K. Swain, S. Devarakonda, and U. K. Madawala, "Modeling, sensitivity analysis, and controller synthesis of multipickup bidirectional inductive power transfer systems," *IEEE Trans. Ind. Informat.*, vol. 10, no. 2, pp. 1372–1380, May 2014.
[21] C. Park, S. Lee, G. H. Cho, S. Y. Choi, and C. T. Rim, "Two-dimensional inductive power transfer system for mobile robots using evenly displaced multiple pickups," *IEEE Trans. Ind. Appl.*, vol. 50, no. 1, pp. 558–565, Feb. 2014.
[22] C. Liu, A. P. Hu, B. Wang, and N. C. Nair, "A capacitively coupled contactless matrix charging platform with soft switched transformer control," *IEEE Trans. Ind. Electron.*, vol. 60, no. 1, pp. 249–260, Jan. 2013.
[23] J. E. James, D. R. Robertson, and G. A. Covic, "Improved AC pick-ups for IPT systems," *IEEE Trans. Power Electron.*, vol. 29, no. 12, pp. 6361–6374, Dec. 2014.
[24] S. Weerasinghe, D. Thrimawithana, and U. Madawala, "Modelling bi-directional contactless grid interfaces with a soft DC-link," *IEEE Trans. Power Electron.*, vol. 30, no. 7, pp. 3528–3541, Jul. 2015.
[25] L. Chen, G. Nagendra, J. Boys, and G. Covic, "Double-coupled systems for IPT roadway applications," *IEEE J. Emerg. Sel. Topics Power Electron.*, vol. 3, no. 1, pp. 37–49, Mar. 2015.
[26] Y. Jang and M. M. Jovanovic, "Contactless electrical energy transmission system having a primary side current feedback control and soft-switched secondary side rectifier," U.S. Patent 6 934 167 B2, Aug. 23, 2005.
[27] E. Asa, K. Colak, M. Bojarski, and D. Czarkowski, "A novel phase control of semi bridgeless active rectifier for wireless power transfer applications," in *Proc. Appl. Power Electron. Conf.*, Mar. 2015, pp. 3225–3231.
[28] K. Colak, M. Bojarski, E. Asa, and D. Czarkowski, "A constant resistance analysis and control of cascaded buck and boost converter for wireless EV chargers," in *Proc. Appl. Power Electron. Conf.*, Mar. 2015, pp. 3157–3161.

Kerim Colak (M'13) received the M.Sc. degree in energy systems engineering from the Gebze Institute of Technology, Izmit, Turkey, in 2004, and the Ph.D. degree in electrical engineering from the Polytechnic School of Engineering, New York University, Brooklyn, NY, USA, in 2013.

His current research interests include isolated and nonisolated dc–dc converters, the system modeling and optimization of railway systems, catenary-free railway vehicles, plug-in electric and hybrid electric vehicles, and wireless energy transfer applications.

Dr. Colak is currently Training & Education Chief in Istanbul Transportation Company, Istanbul, Turkey.

Erdem Asa (S'14) received the B.Sc. (Hons.) and M.Sc. degrees in electrical engineering from Gazi University, Ankara, Turkey, in 2007 and 2009, respectively. He is currently working toward the Ph.D. degree at the Polytechnic School of Engineering, New York University, Brooklyn, NY, USA.

He has authored or coauthored more than 20 journals and conference papers. His current research interests include isolated and nonisolated dc–dc converters, energy management strategies for renewable energy sources, plug-in electric and hybrid electric vehicles, and wireless energy transfer applications.

Mr. Asa received the IEEE Power and Energy Society and Industrial Applications Society, New York Chapter, and the Ph.D. Distinguished Student Award in 2014.

Mariusz Bojarski (M'15) received the M.Sc. degree in electronics and computer engineering from the Warsaw University of Technology, Warsaw, Poland, in 2009, and the Ph.D. degree in electrical engineering from the Polytechnic School of Engineering, New York University, Brooklyn, NY, USA, in 2014.

His current research interests include power electronics, resonant converters, wireless power transfer, and battery chargers.

Dr. Bojarski is currently continuing his post-doctoral research at Polytechnic School of Engineering, New York University, NY, USA.

Dariusz Czarkowski (M'97) received the M.Sc. degree in electronics from the AGH University of Science and Technology, Krakow, Poland, in 1989, the M.Sc. degree in electrical engineering from Wright State University, Dayton, OH, USA, in 1993, and the Ph.D. degree in electrical engineering from the University of Florida, Gainesville, FL, USA in 1996.

He joined the Polytechnic School of Engineering, New York University, Brooklyn, NY, USA, in 1996, where he is currently an Associate Professor of electrical and computer engineering. He is a coauthor of a book *Resonant Power Converters.* Hoboken, NJ, USA: Wiley, 2011. His current research interests include power electronics and power distribution systems. He is serving as an Associate Editor for the *International Journal of Power and Energy Systems*.

Omer C. Onar (M'10) received the Ph.D. degree in electrical engineering from the Illinois Institute of Technology, Chicago, IL, USA, in July 2010.

In July 2010, he joined the U.S. Department of Energy's Oak Ridge National Laboratory (ORNL), Oak Ridge, TN, USA. At ORNL, he has been working on several projects including advanced power electronics and electric drives, renewable energies, energy storage systems, wireless power transfer systems, and smart grids.